

Helical structure of longitudinal vortices embedded in turbulent wall-bounded flow

CLARA M. VELTE, MARTIN O. L. HANSEN
AND VALERY L. OKULOV

Department of Mechanical Engineering, Technical University of Denmark, DK-2800 Kgs.
Lyngby, Denmark

(Received ...)

Embedded vortices in turbulent wall-bounded flow over a flat plate, generated by a passive rectangular vane-type vortex generator with variable angle β to the incoming flow in a low-Reynolds number flow ($Re = 2600$ based on the inlet grid mesh size $L = 0.039$ m and free stream velocity $U_\infty = 1.0 \text{ m s}^{-1}$) have been studied with respect to helical symmetry. The studies were carried out in a low-speed closed-circuit wind tunnel utilizing Stereoscopic Particle Image Velocimetry (SPIV). The vortices have been shown to possess helical symmetry, allowing the flow to be described in a simple fashion. Iso-contour maps of axial vorticity revealed a dominant primary vortex and a weaker secondary one for $20^\circ \leq \beta \leq 40^\circ$. For angles outside of this range, the helical symmetry was impaired due to the emergence of additional flow effects. A model describing the flow has been utilized, showing strong concurrence with the measurements, even though the model is decoupled from external flow processes that could perturb the helical symmetry. The pitch, vortex core size, circulation and the advection velocity of the vortex all vary linearly with the device angle β . This is important for flow control, since one thereby can determine the axial velocity induced by the helical vortex as well as the swirl redistributing the axial velocity component for a given device angle β . This also simplifies theoretical studies, e.g. to understand and predict the stability of the vortex and to model the flow numerically.

1. Introduction

Streamwise vortices embedded in turbulent boundary layers is a common phenomenon and is seen e.g. in the treatment of free organized structures (see e.g. Adrian 2007, and references therein), Görtler vortices in boundary layers over walls of streamwise concave curvature (see Görtler 1955), corner vortices with an axial velocity component, vortex rings near walls and as horseshoe vortices folding around objects attached to a wall (Adrian 2007). Often longitudinal vortices are generated with passive devices called vortex generators. A vortex generator is similar to a wing with a small aspect ratio mounted normally to a surface with an angle of incidence to the oncoming flow. It is designed to overturn the boundary layer flow via large scale motions, thereby redistributing the streamwise momentum in the boundary layer which aids in preventing separation. Vortex generators were formally introduced by H. D. Taylor (see Taylor 1947) as an aid in suppressing separation in diffusers. Many studies have presented (nominal) guidelines for optimizing the effect of forced mixing for these passive devices for varying geometries and flow conditions, (see e.g. Schubauer & Spangenberg 1960; Pearcey 1961; Godard & Stanislas 2006). Further, a review on low-profile vortex generators was written by Lin (2002). The applicability of controlled near-wall vortices in engineering is vast, since vortices can

transport both heat and momentum, aiding in cooling or re-energizing the lowest part of the boundary layer. Being able to control/optimize parameters such as the strength and size of the longitudinal vortices to the existing flow setting is highly desired and it is therefore of interest to develop theories and models which can predict and describe these. Some models have been proposed in order to describe the flow, both theoretically (see e.g. Smith 1994) as well as computationally (see e.g. Liu, Piomelli & Spalart 1996; You *et al.* 2006). The model of Smith (1994) predicts the flow field induced by low-profile triangular vanes (extending approximately to the logarithmic region of the boundary layer) in a zero pressure gradient boundary layer. The method modifies the governing equations based on the scales of the geometry and the oncoming flow. Good agreement is found with experiments, however, this model only treats low-profile devices extending to a fraction of the boundary layer height. Having a similar geometric configuration, Liu *et al.* (1996) introduced vortices numerically using body forces and utilized the fact that the azimuthal velocity distribution of the device-induced vortices is similar to that of Lamb-Oseen vortices. The non-uniform axial component was obtained by introducing a Gaussian distributed streamwise force component. However, this was merely introduced and never motivated more than on a purely empirical basis to compensate for the momentum deficit in the wake of the device.

The main objective of this work is the experimental investigation of device-generated vortices to define helical vortex structures in wall-bounded flow and to create a new model which more correctly can describe the vortex flow. Previously, a lot of experimental work was done describing embedded vortices in boundary layer flows using single point measurement techniques (see e.g. Schubauer *et al.* 1960; Shabaka, Mehta & Bradshaw 1985). However, the development of Stereoscopic Particle Image Velocimetry (SPIV) allows non-intrusive instantaneous measurement realizations of the flow in a plane and is the predominating measurement technique for these investigations today (see e.g. Godard *et al.* 2006; Velte, Hansen & Cavar 2008). SPIV measurements in spanwise planes downstream of a single rectangular vortex generator on a flat plate have been conducted and investigated. This configuration is subject to a parametric study, investigating the effect on the helical vortex when varying the angle of the actuating device to the incoming flow. A turbulent boundary layer profile was considered suitable due to a fuller velocity profile. This also makes the results applicable to flows at more realistic Reynolds numbers. The turbulence level was generated using an inlet grid to yield a high enough turbulence intensity to obtain a turbulent boundary layer profile. Results show that the vortex generator gives rise to longitudinal vortices that possess helical symmetry. A simple theoretical flow model is put forward based on the hypothesis of helical symmetry of the generated vortices and the Gaussian distribution of the vorticity field. The axial and azimuthal vorticity components are coupled according to the definition for helical symmetry of vorticity fields; $\omega_r = 0$ and $\omega_\theta/\omega_z = r/l$, where l represents the helical pitch, see figure 2(b). Even though the vortex generators operated in a turbulent boundary layer, yielding relatively large perturbations, the vortex was observed to be stable in the experiments. None of the previous work has dealt with the helical symmetry of embedded longitudinal vortices and specifically, the longitudinal vortices generated by vortex generators have not previously been known to possess helical symmetry.

2. Experimental method

Consider the test section setup in figure 1. The measurements were carried out in a closed-circuit wind tunnel with an 8:1 contraction ratio and a test section of cross-sectional area 300×600 mm with length 2 m. At the inlet of the test section, a turbulence-

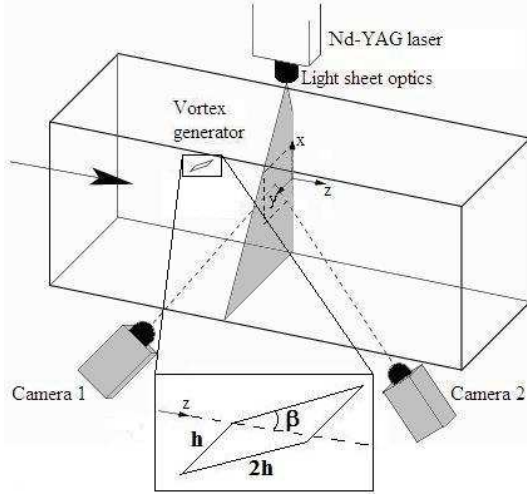


FIGURE 1. Schematic of the experimental set-up and device geometry. The large arrow to the left indicates the main flow direction and β the device angle. The measurement plane in the laser sheet has been indicated by dashed lines.

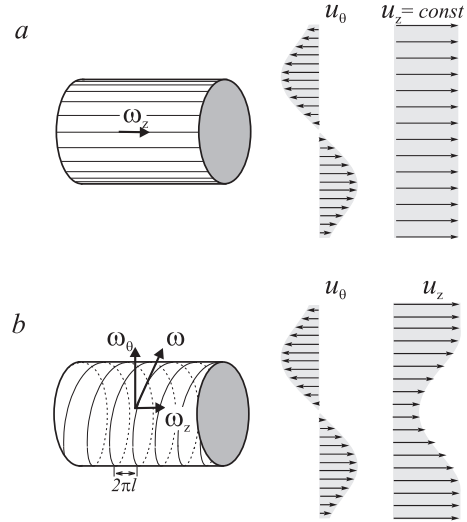


FIGURE 2. Sketch of vorticity field and induced velocity profile by Lamb-Oseen vortex with rectilinear vortex lines (a) and Batchelor vortex with helical structure of vortex lines (b).

generating grid with mesh length 39 mm was situated. The test section had optical access through the top and bottom walls as well as through the sidewall opposite to the wall with the attached vortex generator. The coordinate system is defined in figure 1. z is the axial flow direction, y is the wall-normal direction and x is the spanwise direction.

The experiments were conducted at a free stream velocity of $U_\infty = 1.0 \text{ m s}^{-1}$. The wind tunnel speed was obtained by measuring the pressure drop across an orifice plate. The turbulence intensity at the inlet has from LDA measurements been found to be 13%. The boundary layer thickness at the position of the vortex generator has been estimated from LDA measurements to be approximately $\delta_{VG} = 25 \text{ mm}$. The actuator, as seen in figure 1, is a rectangular vane of the same height as the local boundary layer thickness, $h = \delta_{VG}$, with a length of $2h$. The vortex generator was positioned on a vertical wall in the centre of the test section with its trailing edge 750 mm downstream of the inlet grid when at zero angle to the mean flow. In order to easily and accurately alter the device angle, the vortex generator was attached to a pin which could be accessed from outside of the test section through a hole in the test section wall. This pin was in turn attached to a pointer arm placed over a protractor indicating the relative angle of the actuator to the mean flow direction. The protractor had a radius of 200 mm and grading for integer values of each degree. The device angle of incidence β could therefore be determined with a relatively high accuracy. The measurements were conducted in a spanwise plane, with plane normal parallel to the test section walls, positioned five device heights downstream of the vortex generator. The measurement plane has been indicated by a dashed line in figure 1. Measurements were conducted for $5^\circ \leq \beta \leq 85^\circ$ with 5° angle spacings.

The stereoscopic PIV equipment was mounted on a rigid stand and included a double cavity NewWave Solo 120XT Nd-YAG laser (wavelength 532 nm), capable of delivering light pulses of 120 mJ. The pulse width, i.e. the duration of each illumination pulse, was 10 ns. The light sheet thickness at the measurement position was 2 mm and was created using a combination of a spherical convex and a cylindrical concave lens. The equipment also included two Dantec Dynamics HiSense MkII cameras (1344×1024 pixels) equipped

with 60 mm lenses and filters designed to only pass light with wavelengths close to that of the laser light. Both cameras were mounted on Scheimpflug angle adjustable mountings. The seeding, consisting of DEHS (Di-Ethyl-Hexyl-Sebacin-Esther) droplets with a diameter of 2–3 μm , was added to the flow downstream of the test section in the closed-circuit wind tunnel in order to facilitate a homogeneous distribution of the particles before they enter the test section. The laser was placed above the test section, illuminating a plane normal to the test section walls, see figure 1. The two cameras were placed in the forward scattering direction. The angle of each respective camera to the laser sheet was 45° . The f-numbers of the cameras were set to 2.8, yielding a depth of field which is small but sufficient to cover the thickness of the laser sheet and keeping all illuminated particles in focus while still attaining sufficient scattered light from the tracer particles. In order to avoid reflections from the wall and the vortex generator within the wavelength band of the camera filters, these areas were treated with a fluorescent dye, Rhodamine 6G, mixed with matt varnish to obtain a smooth surface and to ensure that the dye stayed attached. A calibration target was aligned with the laser sheet. This target had a well defined pattern, which could be registered by the two cameras to obtain the geometrical information required for reconstructing the velocity vectors received from each camera to obtain a full description of all three velocity components in the plane. Calibration images were recorded with both cameras at five well defined streamwise positions throughout the depth of the laser sheet in order to capture the out-of-plane component in the reconstructed coordinate system of the measurement plane under consideration. A linear transform was applied to these images for each camera respectively to perform the reconstruction. This procedure was executed both previous to and after the conduction of the measurements to ensure that no drift had occurred. The images were processed using Dantec Dynamicstudio software version 2.0. Adaptive correlation was applied using refinement with an interrogation area size of 32×32 pixels. Local median validation was used in the immediate vicinity of each interrogation area to remove spurious vectors between each refinement step. The overlap between interrogation areas was 50%. For each measurement position, 500 realizations were acquired. The recording of image maps was done with an acquisition rate of 1.0 Hz, ensuring statistically independent realizations based on the convection velocity $U_\infty = 1.0 \text{ m s}^{-1}$ and the mesh size $d = 0.039 \text{ m}$, yielding a time scale of $t = d/U_\infty = 0.039 \text{ s}$. The velocity vector maps contain 73 by 61 vectors. The linear dimensions of the interrogation areas $(x,y)=(1.55,1.04) \text{ mm}$ can be compared to the Taylor microscale and the Kolmogorov length scale estimated to $\lambda_f \approx 9 \text{ mm}$ and $\eta \approx 0.5 \text{ mm}$ from Laser Doppler Anemometry (LDA) measurements (Schmidt 1997).

3. Modelling of the longitudinal vortex

The existence of Lamb-Oseen reminiscent vortex structures embedded in wall-bounded flow has been reported in various experiments and numerical simulations (see e.g. Liu *et al.* 1996). For the Lamb-Oseen vortex, the vorticity is non-zero only for the axial component as (see figure 2(a))

$$\omega_r = 0; \quad \omega_\theta = 0; \quad \omega_z = \frac{\Gamma}{\pi \varepsilon^2} \exp\left(-\frac{r^2}{\varepsilon^2}\right). \quad (3.1a-c)$$

A more general model is the Batchelor vortex (Batchelor 1964), which includes the non-uniform axisymmetrical axial velocity distribution u_z which approaches the Lamb-Oseen vortex in the extreme. This vortex model is commonly used in instability studies of swirling flows (see Heaton & Peake 2007, and references therein). To describe experimental swirl flows (Leibovich 1978; Escudier 1988, Alekseenko *et al.* 1999), the Batchelor

vortex model is usually referred to in the form

$$u_\theta = \frac{K}{r} \left(1 - \exp(-\alpha r^2) \right); \quad u_z = W_1 + W_2 \exp(-\alpha r^2) \quad (3.2a-b)$$

where K , W_1 , W_2 and α are empirical constants with simple physical interpretations as identified by Okulov (1996)

$$\Gamma = 2\pi K; \quad l = K/W_2; \quad u_0 = W_1 + W_2 \quad \text{and} \quad \varepsilon = 1/\sqrt{\alpha} \quad (3.3a-d)$$

where Γ is the vortex strength (circulation), l is the pitch of the helical vortex lines, u_0 is the advection velocity of the vortex and ε is the effective size of the vortex core with Gaussian axial vorticity distribution, see figure 2(b). The profiles given in (3.2) can reproduce experimentally determined swirl flow with high accuracy. One possible approach is to test if the empirical model (3.2) can describe the longitudinal vortex in the present case. However, in accordance with Pierrehumbert (1980) one needs to account for the possible disturbance of the mirror vortex, resulting from the presence of the wall. Another more suitable approach is therefore to extend the Batchelor vortex model to model the flow by helical symmetry of the vorticity, leaving no restrictions on the shape of the vortex core. Flows with helical vorticity can be described by correlation between the axial and circumferential vorticity vector components

$$\omega_r = 0; \quad \omega_\theta = r\omega_z/l; \quad \omega_z = \frac{\Gamma}{\pi\varepsilon^2} \exp\left(-\frac{r^2}{\varepsilon^2}\right) \quad (3.4a-c)$$

with the vorticity vector always directed along the tangent of the helical lines, $x = r \cos \theta$; $y = r \sin \theta$; $z = l\theta$. Flows with helical vorticity can in addition be characterized by the following condition for the velocity field $\vec{u} = \{u_r, u_\theta, u_z\}$.

$$u_z + \frac{r}{l}u_\theta = u_0 \equiv \text{const.} \quad \text{or} \quad u_z = u_0 - \frac{r}{l}u_\theta \quad (3.5a-b)$$

It can be shown that conditions (3.4a-b) and (3.5) are equivalent (see e.g. Okulov 2004). For a flow fulfilling the requirement of (3.5), the main flow parameters are u_0 and l . Sometimes u_0 , u_z and u_θ are found directly from measurements. The pitch l can then be deduced from (3.5), but this approach might lead to an estimate of high relative error if $u_z - u_0$ is small. Multiplying (3.5) by u_z and integrating over the cross-section of the flow one can obtain the pitch through the swirl number S (Alekseenko *et al.* 1999)

$$l = -F_{mm}/(F_m - u_0 G), \quad (3.6)$$

where $F_{mm} = \int_\Sigma \rho u_\theta u_z r d\Sigma$ is the angular momentum flux in the axial direction, $F_m = \int_\Sigma \rho u_z^2 d\Sigma$ the momentum flux in the axial direction, G the flow rate, ρ the fluid density and Σ the cross-section area. All parameters can now be determined: u_0 is found directly from the measurements, l is found through (3.6) and the circulation Γ and the vortex size ε can be extracted from (3.4c). Based on the experimental observation the simple Batchelor vortex model is chosen as

$$u_\theta = \frac{\Gamma}{2\pi r} \left[1 - \exp\left(-\frac{r^2}{\varepsilon^2}\right) \right]; \quad u_z = u_0 - \frac{\Gamma}{2\pi l} \left[1 - \exp\left(-\frac{r^2}{\varepsilon^2}\right) \right]. \quad (3.7a-b)$$

The only requirements of this simple model are the size of the vortex core, the circulation, the helical pitch and the vortex advection velocity.

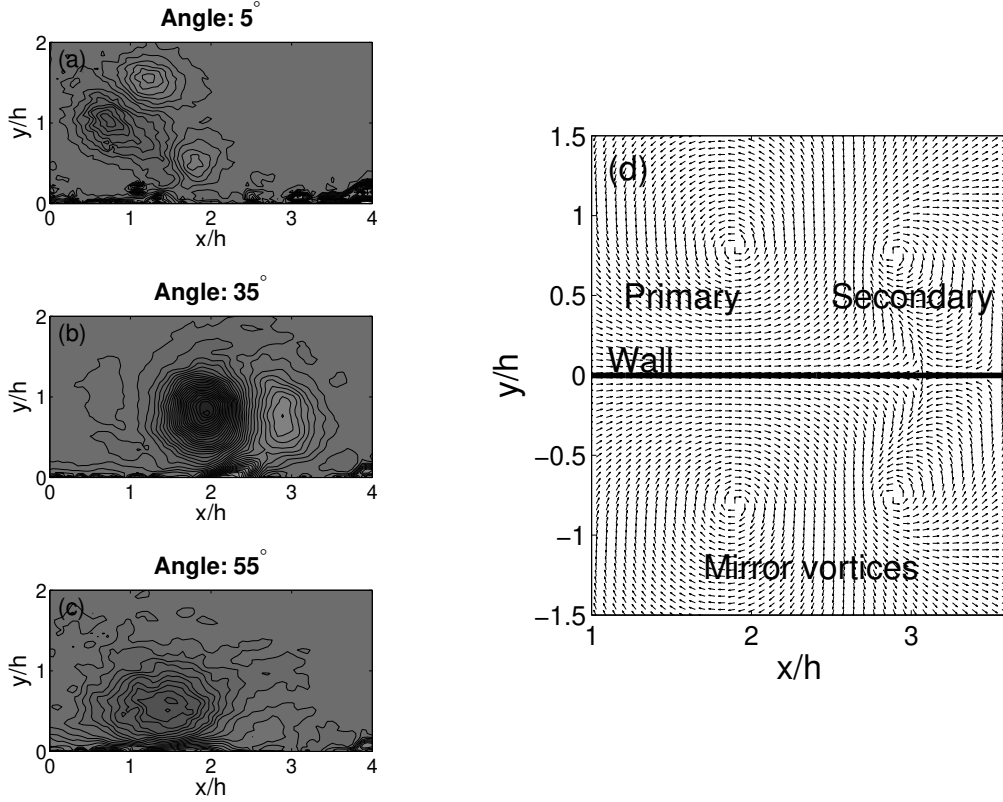


FIGURE 3. Iso-contour maps of axial vorticity for device angles (a) $\beta = 5^\circ$, (b) $\beta = 35^\circ$ and (c) $\beta = 55^\circ$. In (d) a sketch showing a sample velocity distribution of the primary and secondary (upper half) and mirror vortices (lower half) is presented. The wall is illustrated by a thick line at $y/h = 0$.

4. Testing of helical symmetry and embedded columnar vortex flow

The analysis of the embedded vortices was done based on the ensemble averaged complete cross-plane velocity field from the SPIV measurements and the therefrom derived axial vorticity component, see figure 3(a–c). The iso-contour maps of axial vorticity reveal the presence of a secondary vortex, which can be seen next to the main vortex at $x/h \approx 3$ in the iso-contour map for $\beta = 35^\circ$ in figure 3(b). Figure 3(d) displays a sketch of the primary and the secondary vortices in the upper half and the mirrored velocity field in the lower half.

Figure 4 shows the measured axial u_z (upper) and azimuthal u_θ (lower) velocity profiles (+) for various values of the device angle β extracted along a line parallel to the wall through the centre of the primary vortex. Verification of the hypothesis of helical symmetry was done by comparing the left (+) and right (o) hand side of (3.5b) calculated from the measured values of u_z and u_θ . The helical pitch l was found by minimizing the sum of the residuals of the right and left hand side of (3.5b) in a least squares sense for a limited set of points in the radial direction. The values computed from the right hand side (o) are only displayed on the left side of the primary vortex centre, since the flow on the right side is perturbed by the secondary vortex. The two datasets overlap quite well, which is why the difference between the calculated and measured values is hardly visible for some angles.

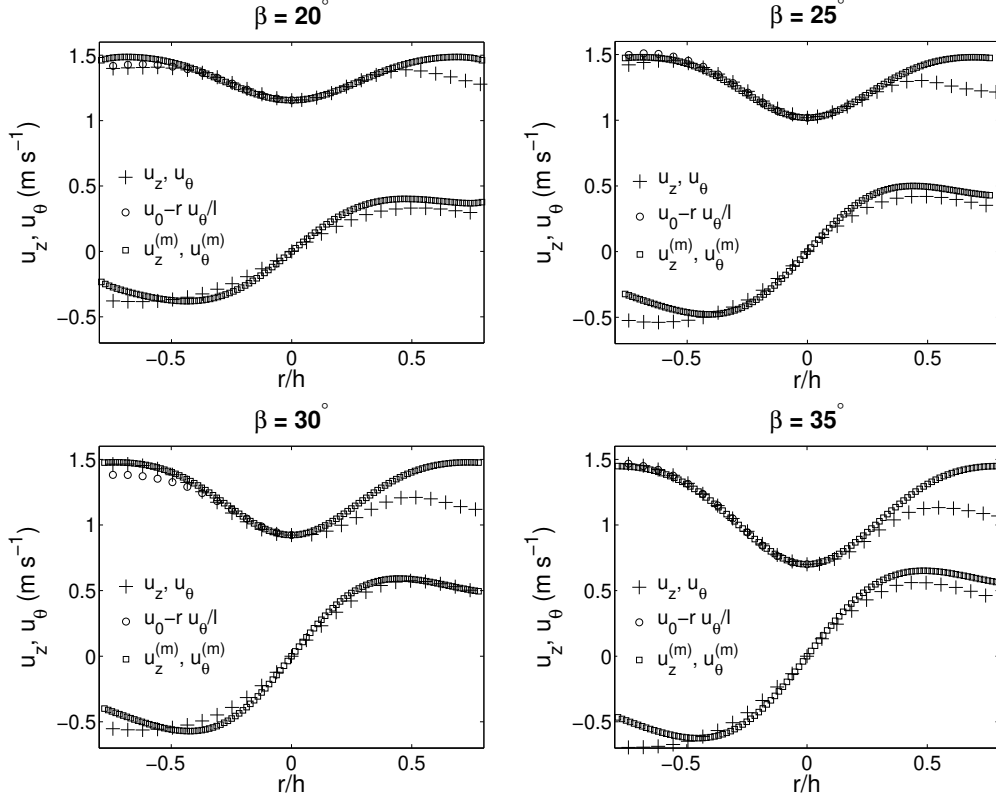


FIGURE 4. Testing of helical symmetry of embedded vortices generated by a vortex generator for various device angles β . The measured axial (u_z , upper) and azimuthal (u_θ , lower) velocity profiles (+) are plotted. The measured values u_z are compared to the right hand side of (3.5b) calculated using the measured values u_θ (o). These computed values are only displayed on the left side, since the flow on the right side is perturbed by the secondary vortex. The two datasets overlap quite well and the difference between the calculated and measured values is hardly visible for some angles. Also displayed are the azimuthal and axial velocity profiles of the utilized vortex model (3.7a–b) (\square).

The axial vorticity fields of the vortices derived from the measurement data have Gaussian distributions and one can therefore use (3.4c) to find the circulation Γ and vortex size ε of both the main and the secondary vortices. The local flow characteristic u_0 was found directly from the measurements and the helical pitch l was obtained from (3.6), yielding a result which agreed well with the values obtained by minimizing the sum of residuals of (3.5b) in a least squares sense. The azimuthal ($u_\theta^{(m)}$) and axial ($u_z^{(m)}$) velocities induced by the main vortex were modelled using (3.7a–b) (\square) and should be compared to the measurements (+), see figure 4. This simple model is decoupled from all additional flow effects such as the secondary and mirror vortices and the non-uniform flow due to the presence of the wall. In spite of this, the model describes the primary vortex flow well in the regime under consideration.

The secondary vortex is present with varying strength at all considered device angles, introducing a disturbance in the flow field of the main vortex and thereby causing asymmetry. The mirror vortices will have the same effect on the symmetry of the main vortex. For angles smaller than 15° , an additional vortex was observed, increasing the complexity of the flow by yielding a three vortex system perturbing the vorticity distribution and

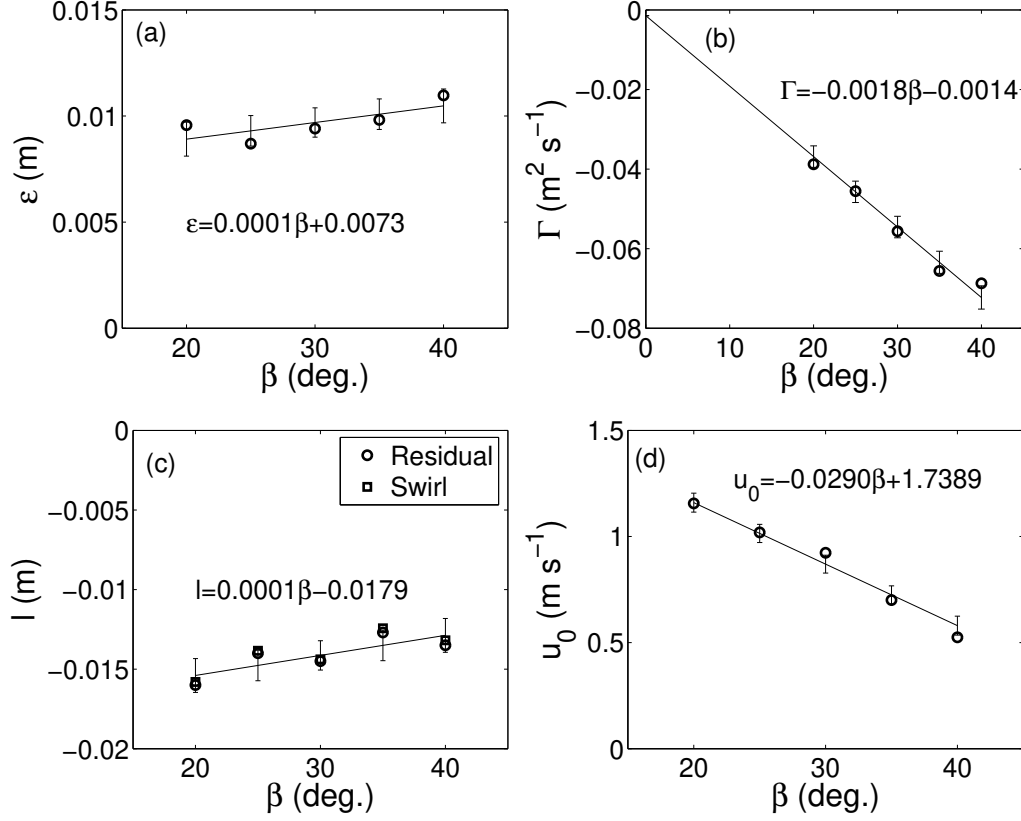


FIGURE 5. Device angle β dependency of (a) the vortex radius ϵ , (b) circulation Γ , (c) helical pitch l and (d) advection velocity of the vortex u_0 . The datasets are provided with a linear fit in a least squares sense with corresponding error bars. In (c), the helical pitch l has been obtained from minimizing the residual of (3.5b) in a least squares sense (\circ) and is compared to the helical pitch of the swirling flow (3.6) (\square) obtained using (3.7a-b).

the velocity field considerably, see figure 3(a). For small values of β , the vortex system becomes more complicated and equation (3.4c) is not representative for the actual flow. For angles larger than 40° , the fit again becomes worse due to the instabilities for high values of circulation at large device angles, see figure 3(c). For increasing values of β , the vorticity component will surpass from streamwise to more and more spanwise, eventually resulting in pure shedding in the extreme $\beta = 90^\circ$. Due to the decreasing longitudinal vorticity component for large values of β , the helical symmetry is destroyed. The deviations arise because we have a simple model with linear interactions, which is being compared to measured values originating from a more complex representation of the flow. Nonlinearities are not captured by the linear model and become increasingly dominant outside of the range $20^\circ \leq \beta \leq 40^\circ$.

Figure 5 shows the device angle dependency of the parameters of the problem in the range $20^\circ \leq \beta \leq 40^\circ$. The device angle dependency of the vortex radius ϵ and circulation Γ , obtained from the Gaussian fit (3.4c) of the vorticity, are shown in figures 5(a) and 5(b) respectively. The datasets have been fitted with a linear approximation in a least squares sense, with corresponding error estimates. For the circulation, the fitting has been extrapolated to zero device angle. As expected, the extrapolated circulation is approximately zero at $\beta = 0^\circ$, since a device with no angle to the flow ideally will not

give rise to any circulation. One can see that the vortex size and the magnitude of the circulation increase linearly with the device angle. The device angle dependency of the helical flow characteristics l and u_0 with linear fitting and error bars are shown in figures 5(c) and 5(d) respectively. In figure 5(c), the values of the helical pitch l obtained from minimizing the residual of (3.5b) in a least squares sense (\circ) are compared to the helical pitch of the swirling flow (3.6) (\square) obtained using the axial and azimuthal velocities of the model (3.7a–b). These two datasets are strongly correlated and it is also seen that the pitch only varies marginally with device angle β . The advection velocity of the vortex u_0 decreases linearly with device angle.

5. Conclusions

Vortices generated by a passive rectangular vane-type vortex generator of the same height as the boundary layer thickness in a flat plate wall-bounded flow have been studied experimentally. It has been shown that the embedded vortices possess helical symmetry in the device angle range $20^\circ \leq \beta \leq 40^\circ$. The flow field in the considered regime consists of two vortices, the primary one and a secondary one. Outside of this range additional flow effects influence the helical vortex in a destructive way, deterring the helical symmetry to persist. The vorticity distribution across the vortices is Gaussian, yielding estimates of the vortex radius ε and circulation Γ through (3.4c). This rendered the possibility to describe the flow in a realistic and simple fashion, utilizing a model for the azimuthal and axial velocity components, (3.7a–b). Comparison of these modelled velocities to the measured data showed to concur well in the device angle regime under consideration. Being the main flow characteristics of a vortex with helical symmetry, the determination of the helical pitch l and the axial velocity at the vortex centre u_0 is of great importance to characterize the vortex (3.5a–b). u_0 was obtained directly from the measurements, whereas the pitch was determined by minimization of the sum of the residuals of (3.5b) in a least squares sense or alternatively from (3.6). The results of these two methods for pitch evaluation showed a high degree of concurrence.

The vortex radius ε , the circulation Γ , the helical pitch l and the advection motion of the vortex (or axial velocity at the vortex centre) u_0 all showed linear dependency with the device angle β . These simple relations render it possible to predict these parameter values for device angles in the range $20^\circ \leq \beta \leq 40^\circ$ well and thereby determine vortex strength, size and axial flow distribution. They also facilitate theoretical studies analysing e.g. stability and aid in modelling the flow within this range. The vortex radius showed a weak increase with increased device angle β , while the circulation Γ showed a large increase in magnitude. The vortex advection velocity u_0 decreased with increased device angle while the helical pitch did not change notably and can, for the purpose of the model, be considered close to constant.

The Danish Research Council, DSF, is acknowledged for their financial support of the project under grant number 2104-04-0020.

REFERENCES

- ADRIAN, R. J. 2007 Hairpin vortex organization in wall turbulence. In *Phys. Fluids* **19**, 041301.
- ALEKSEENKO, S. V., KUIBIN, P. A., OKULOV, V. L. & SHTORK, S. I. 1999 Helical vortices in swirl flow. In *J. Fluid Mech.* **382**, 195–243.
- BATCHELOR, G. K. 1964 Axial flow in trailing line vortices. In *J. Fluid Mech.* **20**, 645–658.
- ESCUDIER, M. P. 1988 Vortex breakdown: observations and explanations. In *Prog. Aerosp. Sci.* **25** 189–229.

- GODARD, G. & STANISLAS, M. 2006 Control of a decelerating boundary layer. Part 1: Optimization of passive vortex generators. In *Aerosp. Sci. Technol.* **10** 181–191.
- GÖRTLER, H. 1955 Dreidimensionales zur Stabilitätstheorie laminarer Grenzschichten. In *ZAMM* **35** 326.
- HEATON, C. J. & PEAKE, N. 2007 Transient growth in vortices with axial flow. In *J. Fluid Mech.* **587**, 271–301.
- KUIBIN, P. A. & OKULOV, V. L. 1996 One-dimensional solutions for a flow with a helical symmetry. In *Thermophys. Aeromech.* **3** 297–301.
- LEIBOVICH, S. 1978 The structure of vortex breakdown. In *Ann. Rev. Fluid Mech.* **10** 221–246.
- LIN, J. C. 2002 Review of research on low-profile vortex generators to control boundary-layer separation. In *Prog. Aerosp. Sci.* **38**, 389–420.
- LIU J., PIOMELLI, U. & SPALART, P. R. 1996 Interaction between a spatially growing turbulent boundary layer and embedded streamwise vortices. In *J. Fluid Mech.* **326**, 151–179.
- OKULOV, V. L. 1996 The transition from the right helical symmetry to the left symmetry during vortex breakdown. In *Tech. Phys. Lett.* **22**, 798–800.
- OKULOV, V. L. 2004 On the stability of multiple helical vortices. In *J. Fluid Mech.* **521**, 319–342.
- PEARCEY, H. H. 1961 Shock induced separation and its prevention by design and boundary layer control. In *Boundary Layer and Flow Control*, ed. Lachmann, G. V., vol. 2, pp. 1166–1344, Pergamon Press, Oxford, Great Britain.
- PIERREHUMBERT, R. T. 1980 A family of steady, translating vortex pairs with distributed vorticity. In *J. Fluid Mech.* **99**, 129–144.
- SCHMIDT, J. J. 1997 Experimental and numerical investigation of separated flows. PhD thesis, Technical University of Denmark, Kgs. Lyngby.
- SCHUBAUER, G. B. & SPANGENBERG, W. G. 1960 Forced mixing in boundary layers. In *J. Fluid Mech.* **8**, 10–32.
- SHABAKA, I. M. M. A., MEHTA, R. D. & BRADSHAW, P. 1985 Longitudinal vortices imbedded in turbulent boundary layers. Part 1. Single vortex. In *J. Fluid Mech.* **155**, 37–57.
- SMITH, F. T. 1994 Theoretical prediction and design for vortex generators in turbulent boundary layers. In *J. Fluid Mech.* **270** 91–131.
- TAYLOR, H. D. 1947 The elimination of diffuser separation by vortex generators. *Research Department Report No. R-4012-3*, United Aircraft Corporation, East Hartford, Connecticut.
- VELTE, C. M., HANSEN, M. O. L. & CAVAR, D. 2008 Flow analysis of vortex generators on wing sections by stereoscopic particle image velocimetry measurements. In *Environ. Res. Lett.* **3** 015006.
- YOU, D., WANG, M., MITTAL, R. & MOIN, P. 2006 Large-eddy simulations of longitudinal vortices embedded in a turbulent boundary layer. In *AIAA Journal* **44** 3032–3039.